

Three Dimensional Multi-layered Graphene and Multi-layer Graphene-CNT Hybrid Materials via Rapid Thermal Annealing of Nickel Acetate as a Pt Nanoparticle Support

Thomas O. M. Samuels¹, Alex W. Robertson¹, Heeyeon Kim², Mauro Pasta¹, and Jamie H. Warner^{1}*

¹Department of Materials, University of Oxford, Parks Road, Oxford, OX1 3PH, United Kingdom

²Energy Materials Lab, Korea Institute of Energy Research, 152 Gajeong-ro, Yuseong-gu, Daejeon 305-343, Korea

*Jamie.warner@materials.ox.ac.uk;

Abstract

Three-dimensionally structured graphitic materials are of interest for electrochemical applications as electrodes and catalyst supports. Many synthetic approaches to these materials require a preformed three-dimensional template and a carbon source, especially when highly crystalline materials are required. In this report, we utilise nickel acetate, which contains both a metal catalyst and a carbon source, as the sole component in the synthesis of both three-dimensional multi-layered carbon and graphene spherical structures (GS) and GS – carbon nanotube hybrid materials (GS-CNT), depending on the annealing procedure. By varying the synthesis conditions of these materials we are able to control the crystallinity of the structures. We show that the rapid introduction of the precursor into the hot zone is a key

factor in the formation of the structures. This method demonstrates the utility of cheap metal salts as the sole component of the scalable synthesis of three-dimensional hybrid graphitic materials. We then utilise the novel materials as supports for platinum (Pt) nanocrystals produced using a thermal annealing approach and compare the effect of the carbon support on the active surface area and durability in cyclic voltammetry experiments.

KEYWORDS: Graphene, carbon nanotubes, platinum, fuel cell, graphene sphere

Introduction

Graphene consists of a single layer of sp^2 bonded carbon atoms and is of interest as an electrode material for electrochemical energy generation and storage. This is because graphene has exceptional thermal and electrical conductivity, good chemical stability and a high surface area,¹ making it ideal for use in fuel cells,² batteries³ and supercapacitors.⁴ One issue surrounding the use of individual graphene sheets, such as those produced using chemical exfoliation and subsequent reduction from graphene oxide, is the tendency to re-stack over time, which lowers the surface area of the material and can make active sites of other materials supported on graphene inaccessible, leading to a loss of activity over time.⁵ Recent research has focused on the production of three-dimensionally structured graphene materials which are more resistant to stacking.⁶ Mass producing high quality three-dimensional graphene is still challenging however. In the chemical vapour deposition method, a gaseous source of carbon breaks down on the surface of the metal template.⁷ Another option is the annealing method, where a mixture of a metal template (most often nickel) and a carbon source is heated, the carbon source dissolves in the nickel and forms graphene upon cooling.⁸ Both these methods require a pre-formed metal template, which increases the number of steps required to synthesise 3D graphene and increases cost.

Another strategy for enhancing the utility of graphene in electrochemical applications is the combination of CNTs, these act to enhance the conductivity of the graphene materials and prevent re-stacking.⁹ This either requires the subsequent growth of CNTs on the graphene materials¹⁰ or the mixing of CNTs and graphene grown separately,^{11, 12} increasing the number of steps and processing required.

In this report we utilise nickel acetate, a readily available and cheap nickel compound, to form both the nickel template/catalyst and carbon source in-situ when rapidly heated in an inert atmosphere. By controlling the annealing temperature, we show that it is possible to form both high quality multi-layered graphene shells (GS) and a combination of graphene shells and cup-stacked carbon nanotubes (GS-CNT) using a single precursor.

One important application of 3D carbon materials is as a catalyst support for platinum (Pt) nanoparticles, which are important catalysts for the hydrogen oxidation (HOR) and oxygen reduction (ORR) reactions in PEMFC fuel cells, as well as the hydrogen evolution reaction (HER) for the production of hydrogen.^{13, 14} To explore the novel materials produced, Pt nanoparticles are then grown on the different carbon supports using a thermal annealing method. Their electrochemically active surface area and durability are then compared in cyclic voltammetry experiments.

Results and Discussion

Previous experiments have shown that above 350 °C nickel acetate decomposes into nickel (with residual carbon), some nickel oxide (which is reduced to nickel by other decomposition products at higher temperatures), and a mixture of gases which include H₂O, H₂, CO, CH₄ and other small organic molecules.¹⁵ These are gases which are commonly utilised in chemical vapour deposition (CVD) processes for the growth of carbon materials on metal

surfaces. CH₄ has been commonly utilised as a carbon source in CVD processes for the growth of both carbon nanotubes¹⁶ and graphene.¹⁷ CO is also used as a fuel for the growth of carbon nanotubes.¹⁸ H₂ plays an important role in the synthesis of graphene, where it acts to aid CH₄ decomposition on the surface of nickel.¹⁹ For the formation of CNTs, hydrogen can play an important role in determining the resulting morphology.²⁰ Nickel has been extensively explored as a catalyst for the growth of carbon nanomaterials; carbon dissolves in nickel at elevated temperatures, which can then precipitate out as graphitic layers upon cooling.²¹ Previous studies have taken advantage of this to synthesise both 2D and 3D graphene structures using solid precursors by mixing nickel particles²² or foils²³ with polymer. The decomposition of nickel acetate is thought to take place via a metastable Ni₃C phase.^{24, 25} A recent study indicates that this phase readily decomposes into amorphous carbon and a carbon-rich Ni phase.²⁶ This amorphous carbon can be graphitised at higher temperatures, with some additional carbon precipitating from the nickel particles upon cooling.

We decided to explore the growth of 3D graphitic materials using nickel acetate as the sole catalyst and carbon source, and attempt to utilise the gaseous decomposition products as a carbon source in addition to the carbon residue dissolved in the nickel during decomposition. Samples of nickel acetate were rapidly introduced to a range of temperatures (350-1000 °C) in an argon atmosphere using a furnace on rails, this allowed the sample to be moved in and out of the hot zone of the furnace quickly, allowing for rapid heating and cooling of the sample. A schematic diagram of the furnace system can be seen in Figure S1. Following the annealing process (2 hours), a wet chemical etching method was used to remove as much nickel as possible, to leave hollow carbon structures.

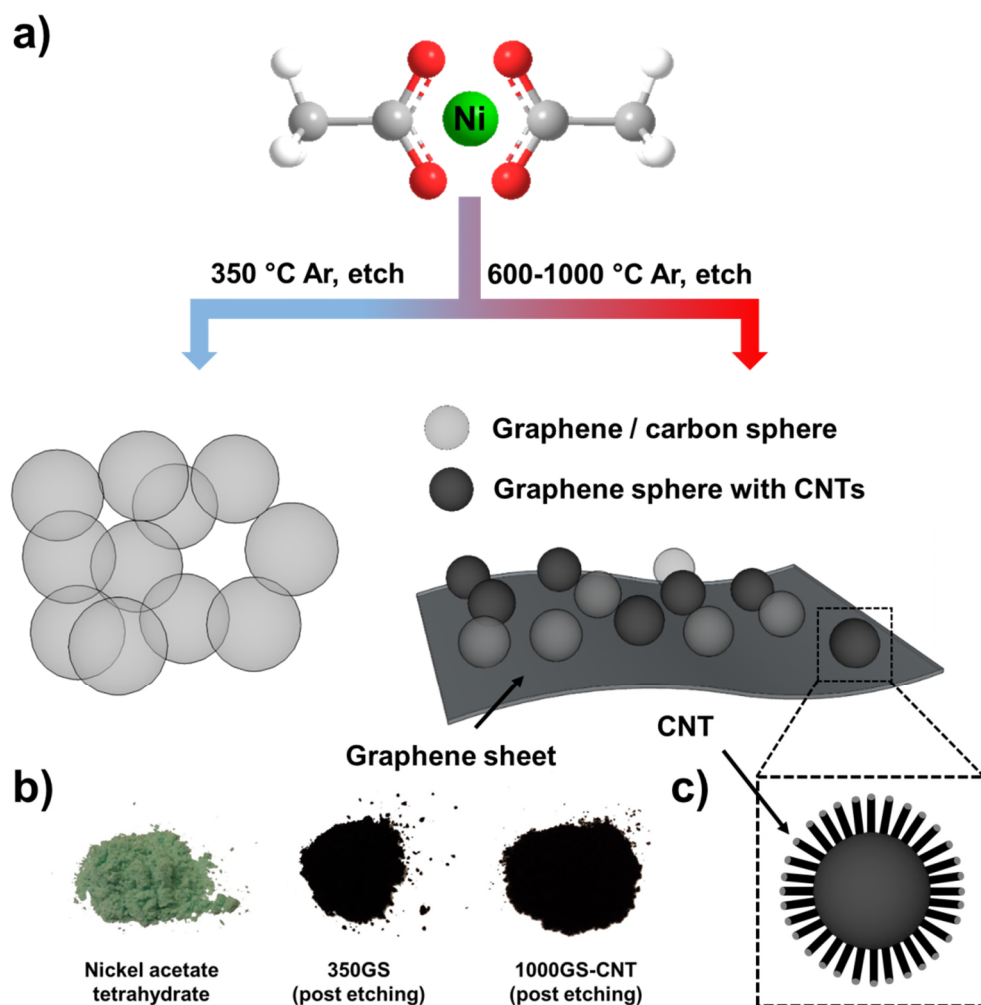


Figure 1. a) Schematic diagram showing the synthesis of GS and GS-CNT from nickel acetate. b) Photographs of the starting material and products following etching. c) Schematic of the CNT-graphene spheres which comprise parts of the GS-CNT samples.

Figure 1 shows a schematic diagram illustrating the synthesis of the material along with pictures of the reactant and products, and how the resultant morphology of the carbon material obtained following etching depends on the annealing temperature. It can be seen from Figure 1b that an obvious physical change has occurred following the annealing and etching procedures, going from green nickel acetate to a black powder. Figure 2 shows SEM and TEM images of the materials produced using the different heating procedures. Annealing at 350 °C, the lowest temperature at which the acetate group decomposes into

nickel (with dissolved carbon), nickel oxide, and gaseous products, yields aggregates of conjoined spherical particles, the SEM of which can be seen in Figure S2. Figure 2a, d and g show SEM and TEM images of the material which reveals that hollow, spherical particles (350GS) remain after etching, presumably carbon precipitated from spherical nickel particles which are removed during the etching process.

When the same procedure is carried out at higher temperatures (600-1000 °C), the structure of the material produced is more complex, and a mixture of different morphologies of carbon materials are produced. Figure 2b and c shows SEM images of different regions of the sample produced at 1000 °C, which indicates that some regions of the sample contain CNTs, whilst others contain spherical particles following etching (pre-etching images can be seen in Figure S3). TEM images of a region of the sample containing the CNTs are seen in Figure 2e and h; these reveal that the tubular structures have grown off spherical particles, similar to those seen in 350GS. TEM images of the regions of the sample without the CNTs (Figure 2f, i) show only spherical particles. Some of the regions comprising spherical particles indicate that they are linked together by larger graphene sheets, the wrinkles of which can be seen in Figure 1f. TEM images of other regions showing graphene sheets are shown in the supporting information (Figure S4). It was observed that the regions of the sample containing CNTs reside at the top of the product in the crucible following annealing, whilst at the bottom of the sample only particles were found. SEM images before etching showing areas of the sample produced at 600 °C (600GS-CNT) demonstrate this (Figure S5). SEM and TEM images of the etched samples produced at 600 °C are shown in Figure S6, it should be noted that the amount of tubular structures seen at 600 °C is lower than observed at 1000 °C, and there is a lack of graphene sheets that are seen in the 1000 °C sample.

Despite an aggressive chemical etching process (see Experimental section), not all the nickel is removed by the hydrochloric acid (HCl). Thermogravimetric analysis (TGA)

measurements indicate that most samples contain residual nickel; for 350GS, 600GS-CNT and 1000GS-CNT these values are 0.5, ~5 and ~10 % weight respectively. This increase in nickel content post-etching with annealing temperature is likely to be due to the multi-layered nature of the graphene shells and their crystallinity at higher temperatures. With higher annealing temperatures nickel particles with dissolved carbon will sinter into larger ones, producing thicker graphene shells upon cooling. Furthermore these layers are more crystalline and will act to protect nickel particles from the acidic environment of the etchant. Figure S7 shows a high resolution TEM (HRTEM) image of a crystal which was not removed during the etching process (1000GS-CNT). The lattice fringes measured in the crystal correspond to the (111) spacing of nickel,²⁷ indicating that the residual nickel has not been converted to nickel chloride (NiCl₂) by the HCl. These thicker, more crystalline layers and residual nickel particles also explain the surface areas of the materials as measured using the Brunauer-Emmett-Teller (BET) method. The measured surface areas of 350GS, 600GS-CNT and 1000GS-CNT were measured as 284, 188, and 110 m²g⁻¹ respectively. A summary of BET results for all samples can be found in Table S1. These surface areas are typically lower than 3D structured graphene powders, which typically have thinner walls than the structures produced using our method. This is most likely due to the high carbon solubility in nickel and the contribution from the metal which remains after etching. It is possible that materials with higher surface areas could be obtained from metal acetates where the metal has a lower carbon solubility, such as copper acetate. Another strategy could be to include other cheap metal precursors which do not contain carbon sources, such as nickel chloride (NiCl₂) in order to increase the metal/carbon ratio.

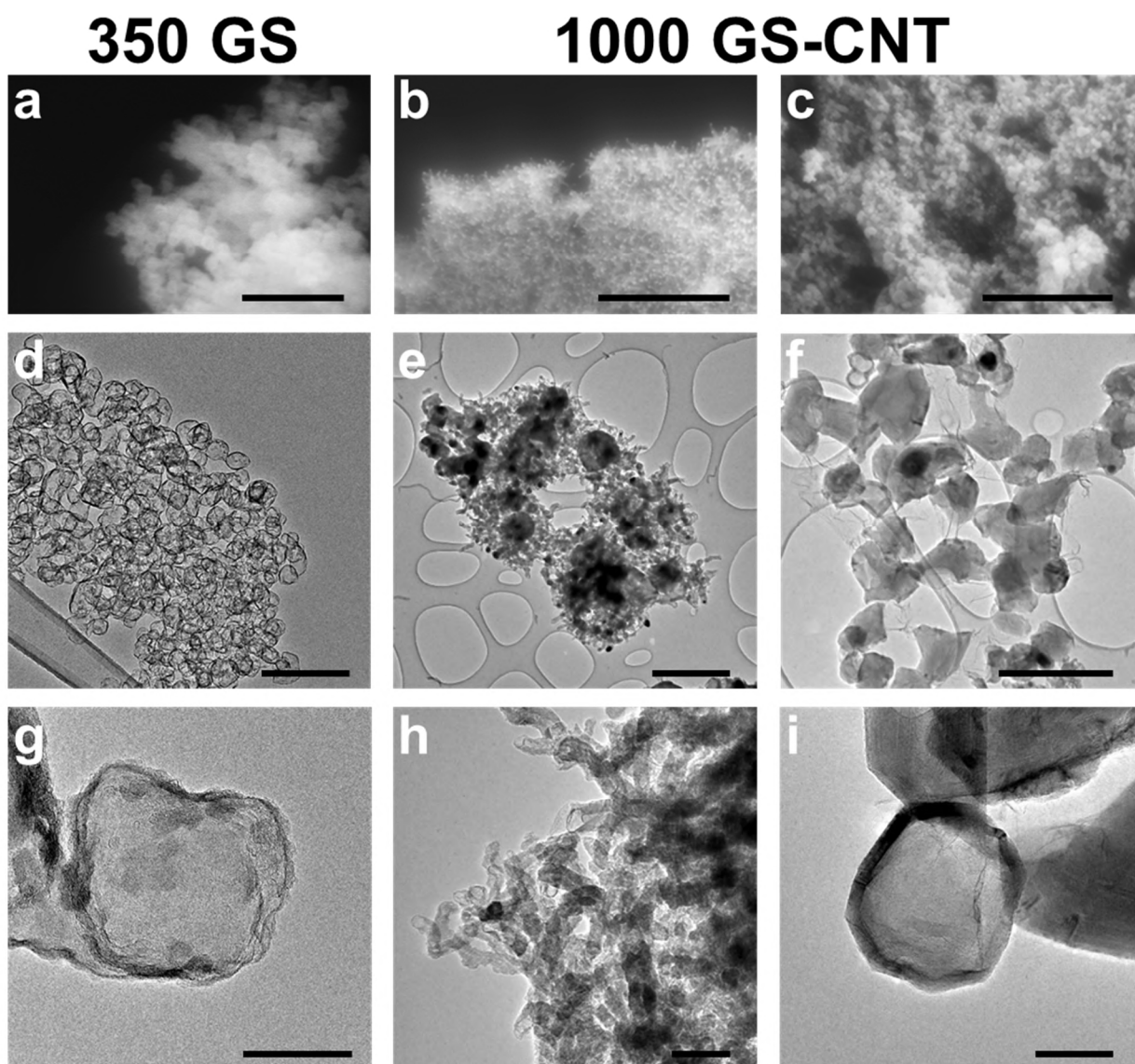


Figure 2. GS and GS-CNT materials following etching (a) SEM image of 350GS (b) SEM image of CNTs in 1000GS-CNT (c) SEM image of particles in 1000GS-CNT (d) low magnification TEM image of 350GS (e) low magnification TEM image of a CNT containing region of 1000GS-CNT (f) low magnification TEM image of graphene spheres without CNTs in 1000GS-CNT (g) TEM image of a graphene sphere in 350GS (h) TEM image of CNTs in 1000GS-CNT (i) TEM image of a graphene sphere in 1000GS-CNT. Scale bars: (a) 1 μm (b) 2.5 μm (c) 2.5 μm (d) 500 nm (e) 500 nm (f) 1 μm (g) 50 nm (h) 50 nm (i) 50 nm.

In order to evaluate the quality of graphene produced in the thermal annealing process, HRTEM and Raman spectroscopy measurements were recorded of the GS-CNT materials produced at different temperatures (600-1000 $^{\circ}\text{C}$) (Figure 3). Closer examination of the CNTs reveals that they are carbon nanotubes with multilayer walls with the cup-stacked

morphology. Black arrows in Figure 3b indicate where the edges of the stacked-cups have reconstructed to form loops, this reconstruction has been reported to produce nanotubes with a comparable electrical conductivity to multi-walled CNTs.²⁸ Measurements of the lattice spacings between the graphene layers for the graphene spheres (Figure 3c) and the CNTs (Figure 3d) gives a value of 0.34 nm, which is the value expected for pristine material.²⁹ Furthermore the moiré pattern can be seen from the graphene sphere in Figure 3c, which is also indicative of highly crystalline material.³⁰ HRTEM images were also recorded of 600GS-CNT (Figure S8), where the measured value of interlayer spacing was larger than 0.34 nm for both the graphene shells (0.36 nm) and CNTs (0.42 nm), indicating that lower quality material was formed when a lower annealing temperature was used.

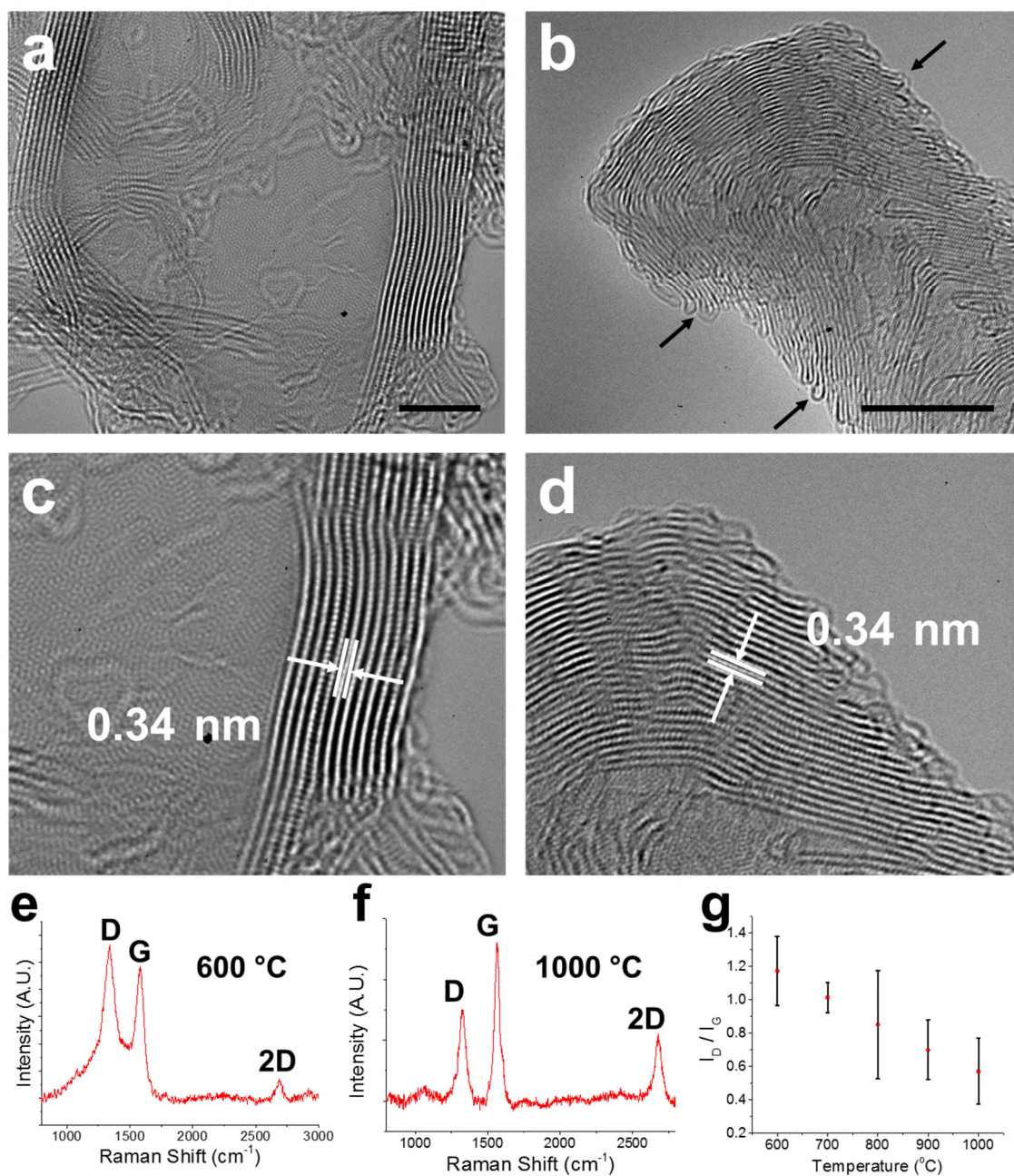


Figure 3. (a) HRTEM image showing a graphene shell from 1000GS-CNT. (b) HRTEM image showing the end of a CNT in 1000GS-CNT, the black arrows indicate the reconstructed loops of the stacked-cups comprising the nanotube (c) HRTEM showing the wall of the graphene shell shown in (a), the interlayer spacing is shown and the moiré pattern is visible. (d) HRTEM image of showing the wall of the CNT shown in (b), with the interlayer spacing shown. (e) Raman spectra of 600GS. (f) Raman spectra of 1000GS-CNT. (g) Graph of I_D/I_G versus the synthesis temperature for structures produced from nickel acetate with an annealing time of 2 hours. Scale bars: (a-b) 10 nm.

The quality of the GS-CNT structures was also evaluated by Raman spectroscopy. The Raman spectra of the sample produced at 600 °C (Figure 3e) indicates carbon with poor

crystallinity. The D peak is higher in intensity than the G peak, indicating a high concentration of defects. In contrast, the D peak is much lower in intensity relative to the G peak in samples produced at 1000 °C, indicating higher quality (Figure 3f). A noticeable D peak is still present, part of which is due to contributions from the carbon nanotubes, which have significant D peaks even for high quality samples.³¹ Raman spectra of samples produced at intermediate temperatures were also recorded, and Figure 3g shows that the I(d)/ I(g) peak ratios strongly correlate to the synthesis temperature, indicating that the quality of the structure produced can be controlled using this thermal annealing method.

Annealing time was also investigated as a method of controlling the quality of the carbon structure. SEM, TEM and Raman results for the product obtained after nickel acetate was annealed for just 10 minutes instead of 2 hours can be seen in Figure S9. These results indicate that the morphology of the product is determined very early in the annealing process, as SEM images indicate an indistinguishable morphology to that obtained with longer annealing times. However, the Raman spectrum indicates a much more defective structure, showing that annealing time can also be used to control the defectiveness of the multilayer graphene structures whilst keeping a similar morphology.

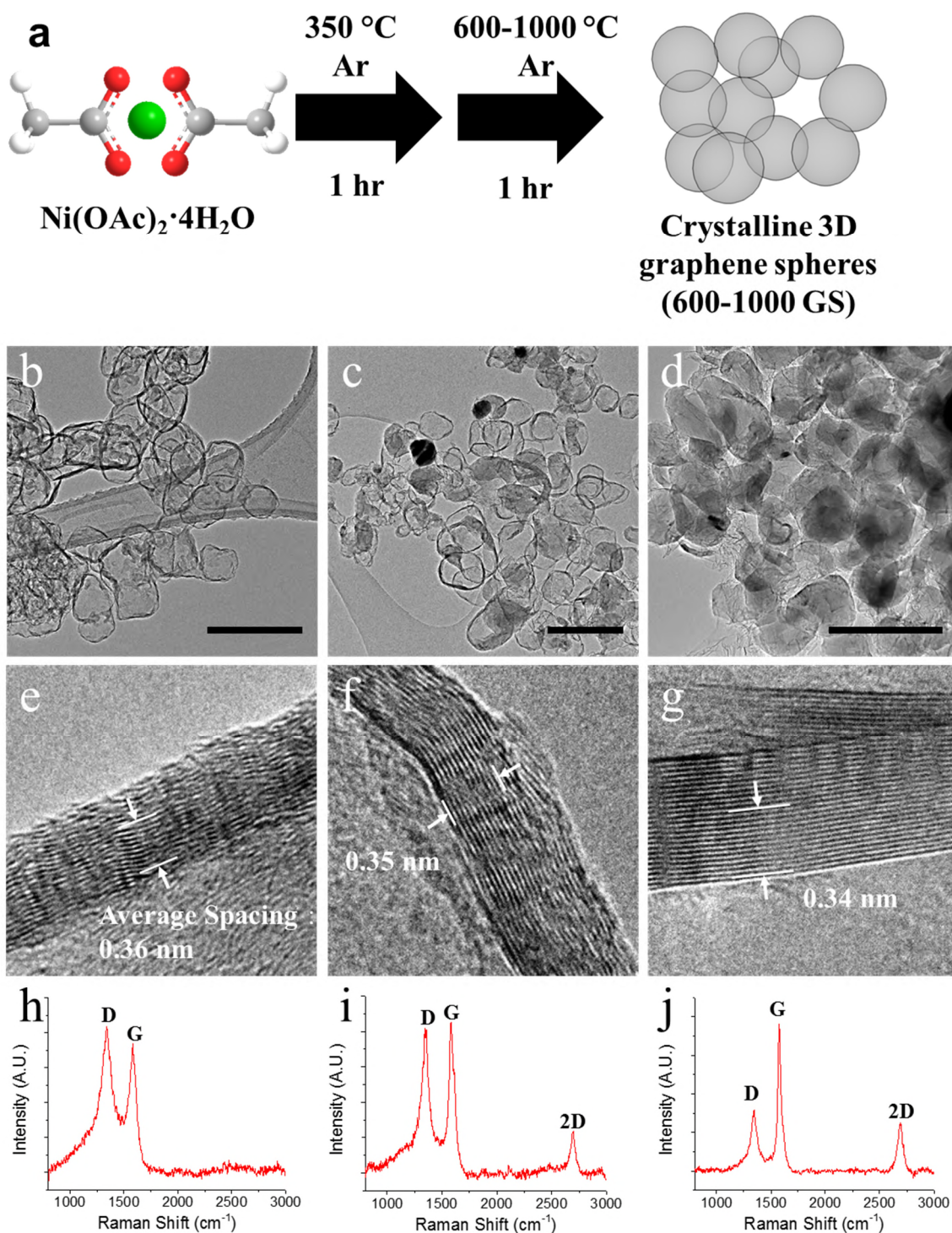


Figure 4. a) Schematic diagram showing the two-stage heating process to produce crystalline graphene spheres (b-d) Low magnification TEM images showing the graphene shells in a) 350GS b) 600GS and c) 1000GS. (e-g) High magnification TEM images showing the walls and average graphene interlayer spacing in d) 350GS e) 600GS and f) 1000GS. (h-j) Representative Raman spectra of h) 350GS i) 600GS and j) 1000GS. Scale bars: (b-d) 250 nm.

In order to attempt to exclusively produce graphene spheres with high crystallinity whilst avoiding the formation of CNTs, a two phase annealing method was adopted. The nickel acetate was introduced into the hot zone of the furnace at 350°C, following one hour of annealing the temperature was increased (50 °C/min) to 600 and 1000 °C, with a total annealing time of two hours (600GS and 1000GS). SEM, TEM and Raman results from the etched samples, along with the results from 350GS can be seen in Figure 4. Similarly sized structures are found in all three samples; the average diameter of the spherical graphene structures are 129, 111 and 134 nm for 350GS, 600GS and 1000GS respectively, though larger particles with diameters of several hundred nanometres, presumably formed through sintering, are seen when the annealing temperature is increased. The interlayer spacings reflect the increase in quality with increased temperature, as the spacing decreases from 0.36 to 0.34 nm when the synthesis temperature is increased from 350 to 1000 °C (Figure 4e-g). This is further corroborated by representative Raman spectra of the samples, showing a decreasing D peak and the emergence of the 2D peak with increasing temperature (Figure 4h-j). The BET surface area decreases as the crystallinity increases, the surface areas of the graphene sphere materials are 284, 229 and 71 m²g⁻¹ for 350GS, 600GS and 1000GS, respectively. This shows that it is possible to selectively avoid the synthesis of the nanotubes whilst achieving high quality multi-layered graphene. Similar structures have been formed using preformed nickel nanoparticles and an external carbon sources in the form of polyols or poly (methyl methacrylate) and the resulting graphene shell structures were shown to be effective structures for lithium-ion storage.^{22, 32}

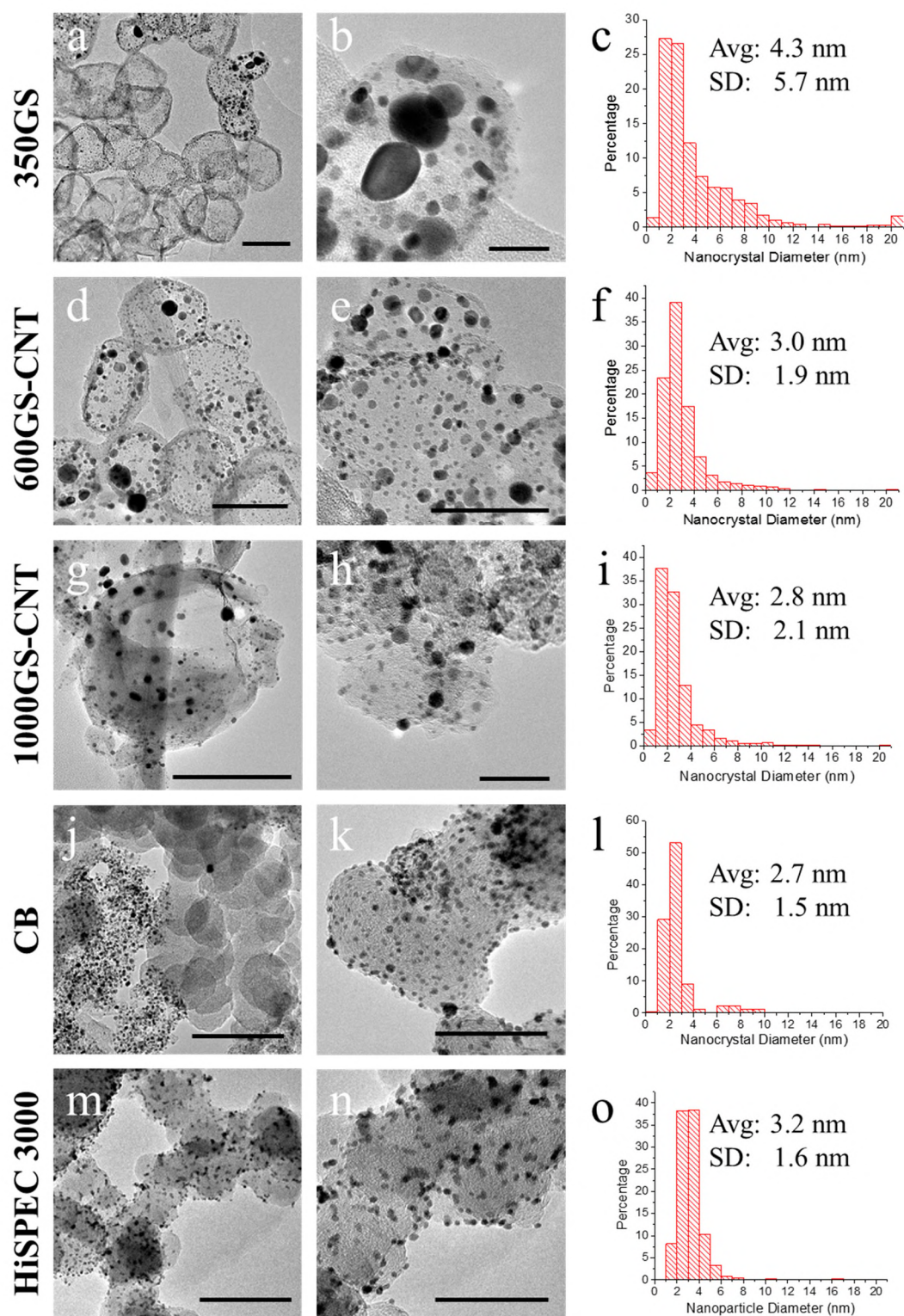


Figure 5. TEM of as-fabricated catalysts. Low magnification images, high magnification TEM images and particle size histograms with averages and standard deviations for 350GS (**a-c**), 600GS-

CNT (**d-f**), 1000GS-CNT (**g-i**), CB (**j-l**) and HiSPEC 3000 (**m-o**). Nanoparticles with >20 nm diameter are grouped for clarity. Scale bars: (a) 100 nm (b) 50 nm (d) 100 nm (e) 50 nm (g) 100 nm (h) 50 nm (j) 100 nm (k) 50 nm (m) 100 nm (n) 50 nm.

In order to understand the formation mechanisms of these materials, a slow heating procedure was used to try and form 1000GS-CNT instead of rapid heating. Figure **S10** shows SEM images of the structures obtained when the nickel acetate is heated at 50 °C/min, rather than sudden introduction into the hot zone of the furnace. Significant portions of the structure have sintered together to form large chunks of nickel and no nanotubes can be seen in the sample. It is likely that, in the slow annealing procedure, all the carbon containing gases have been removed from the furnace long before the nickel reaches the temperature required to catalyse the formation of nanotubes. Any graphene formed during this process likely comes from the carbon dissolved in nickel during the gradual heating. The growth of CNTs using nickel as a catalyst relies on the precipitation of carbon from one side of a nickel particle as more carbon dissolves in the opposite side.¹⁶ This requirement for a constant supply of carbon suggests that the carbon containing gases produced during the acetate decomposition step are utilised by the nickel particles to form the CNTs. To confirm the utilisation of the acetate decomposition products by the nickel particles, the weights of 350GS, 600GS-CNT and 1000GS-CNT were compared before and after chemical etching. It was found that 5.2 wt% of the nickel-carbon product after synthesis was retained following the chemical etching process for 350GS. For 600GS-CNT and 1000GS-CNT, the etched products were found to have retained 6.6 % and 14.3 % of the pre-etching weight respectively. This takes into account the differences in remaining nickel, as determined by TGA. This suggests that more carbon from the acetate decomposition products is retained when the sample is introduced into the hot zone at a higher temperature. A calculation

indicates that if the carbon dissolved in nickel was the sole carbon source, the yield post-etching would be ~6.4% compared to pre-etching, assuming a stoichiometry of Ni_3C , nickel carbide. This implies that at low annealing temperatures, all of the carbon in the product comes from the carbon retained by nickel during decomposition, whereas at an annealing temperature of 1000 °C most of the carbon is from gases generated during decomposition. The fact that the wt% carbon is lower for 350GS compared to the % carbon for the nickel carbide described in the literature may be due to removal of carbon from the nickel by hydrogen gas produced during decomposition, which may not occur when nickel acetate is heated up slowly.

The presence of CNTs and larger graphene sheets in 1000GS-CNT instead of just spheres in 350GS can be explained as follows; when the nickel acetate is introduced at a higher temperature into the hot zone of the furnace, increased sintering of the particles occurs, generating large particles of nickel which form the larger graphene spheres, some of which break into the sheets observed in 1000GS-CNT. However, the nickel on the top of the sample reaches the necessary temperature to catalyse the formation of graphitic structures in a shorter amount of time, which allows more carbon from the decomposition of acetate groups in the lower regions of the sample to be utilised relative to the annealing process at lower temperatures, which allows the formation of carbon nanotubes. This also explains the lower proportion of nanotubes seen in samples at lower temperatures, such as at 600 °C where fewer nanotubes are seen.

There is also some evidence that the rapid introduction into the furnace plays a role in determining the porosity of the structures. Figure S11 shows product obtained from samples of nickel acetate annealed at 350 °C for 20 minutes, which is the shortest amount of time needed for decomposition at this temperature judging by visual appearance. In one case the nickel acetate was dehydrated beforehand via heating in an inert atmosphere at 100 °C, prior

to rapid introduction at 350 °C. This allowed water to be removed from the precursor without any decomposition of the acetate group. SEM images in both samples show obvious differences, with the dehydrated sample having larger aggregates than the hydrated one and fewer obvious holes (Figure S11a-d). TEM images show that for both samples particles with large and small sizes have been formed (Figure S11e-f). Black arrows mark holes that are seen in the aggregates of small particles, which are regularly seen in the hydrated sample but not in the dehydrated sample (Figure S11g-j). It can be assumed that the departure of water during the earliest stages of the annealing procedure is responsible for creating space between the newly forming nickel particles.

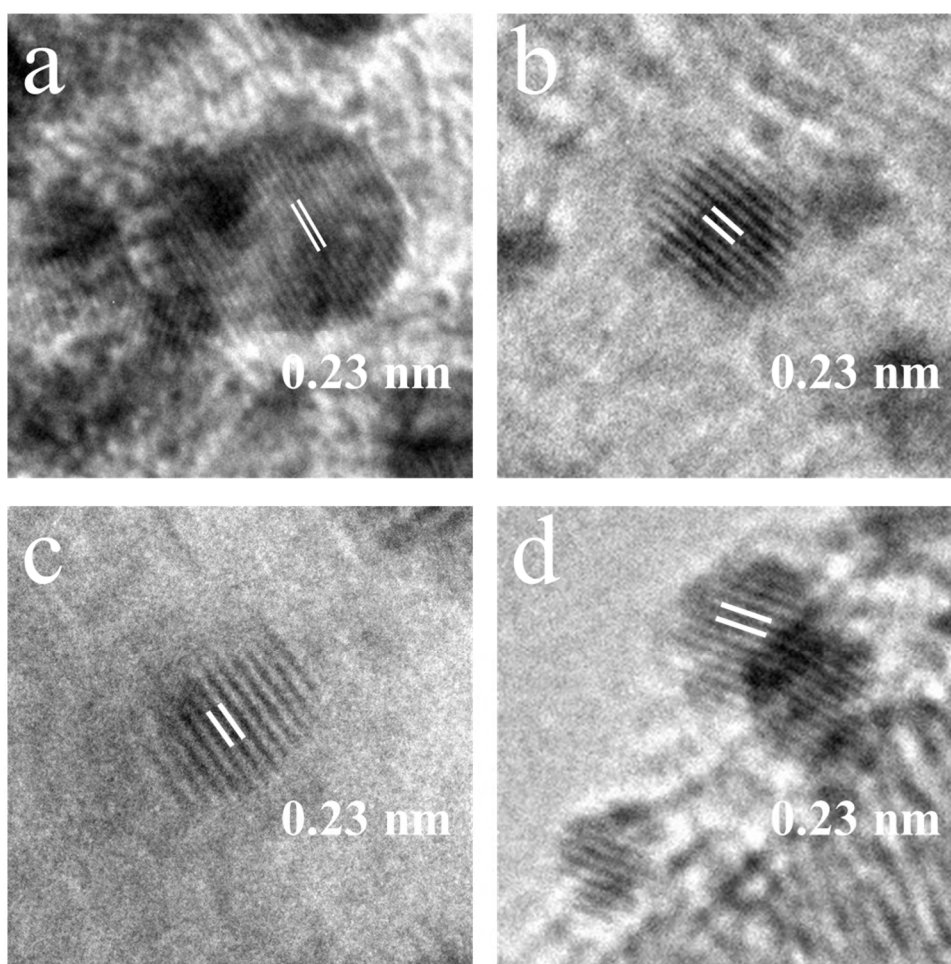


Figure 6. HRTEM images of Pt Nanocrystals synthesised on a) Vulcan XC-72R b) 350GS c) 600GS-CNT d) 1000GS-CNT. The white bars and measurement corresponds to the (111) lattice spacing of Pt.

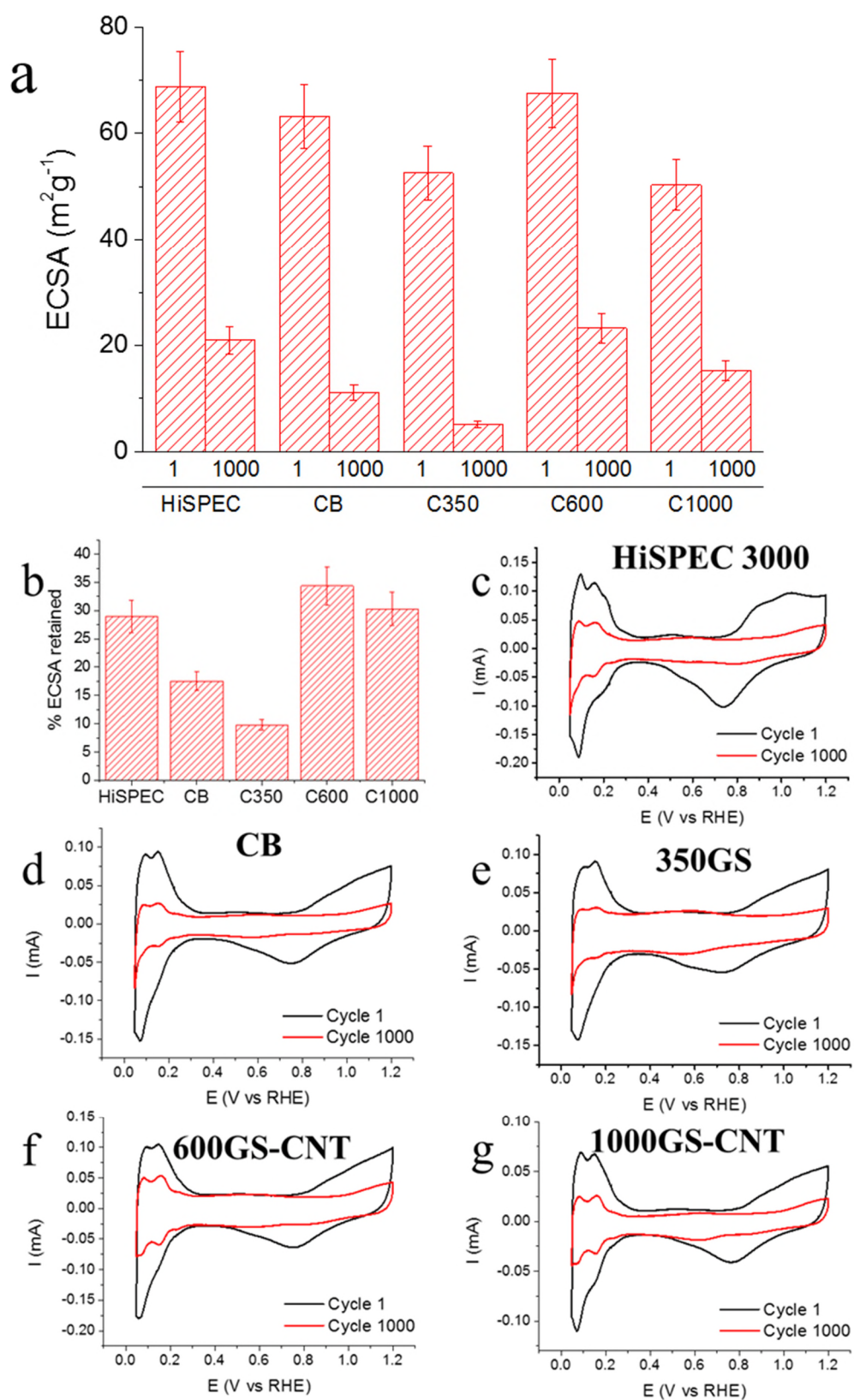


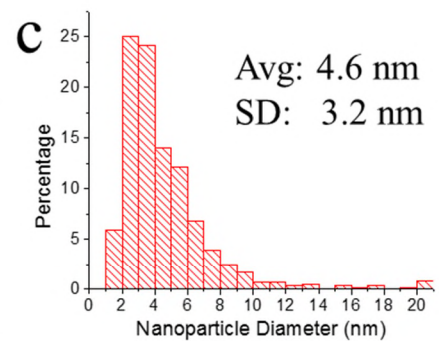
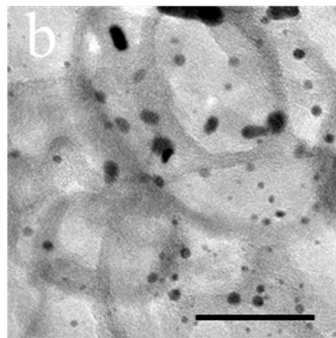
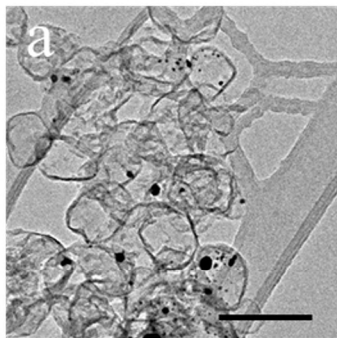
Figure 7. Electrochemical testing of Pt/C catalysts. a) Initial (1st cycle following activation) and final (1000th cycle) ECSAs for all tested catalysts. Error bars for HiSPEC 3000 represent the standard

deviations, while error bars for other samples are estimated based on the HiSPEC standard deviation. b) Graph showing the % ECSA retained by the catalysts after 1000 cycles, the error bar for HiSPEC is the standard deviation which was used to estimate the error in other samples. c-g) Cyclic voltammograms showing the initial and final voltammograms for HiSPEC 3000, CB (Vulcan XC-72R), 350GS, 600GS-CNT and 1000GS-CNT respectively.

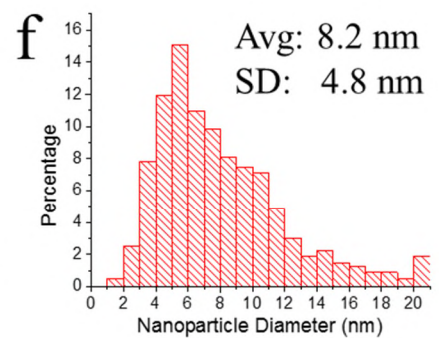
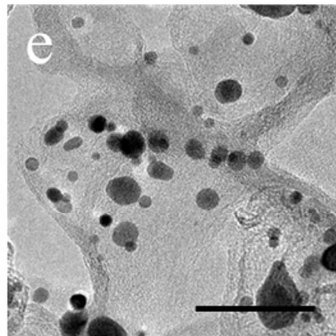
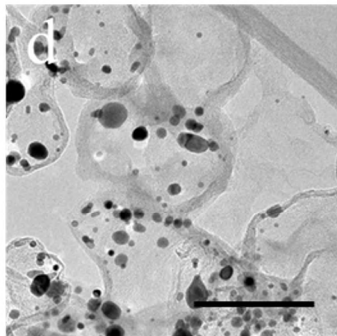
In order to demonstrate the use of the novel carbon materials, 350GS, 600GS-CNT and 1000GS-CNT along with commercial carbon black (CB, Vulcan XC-72R) were utilised as catalyst supports for Pt crystals synthesised using a thermal annealing (TA) approach. In the TA synthesis method, the carbon support is mixed with H_2PtCl_6 precursor solution and left to dry. The resultant powder is then annealed at 400 °C in a reducing atmosphere (H_2/Ar) to form Pt crystals over the surface of the support. Previous work indicates this takes place via a mechanism where individual atoms move over the carbon surface before colliding to form clusters.³³ High magnification TEM image of Pt nanocrystals produced by this method on different carbon supports can be seen in Figure 6. The measured lattice spacing of 0.23 nm corresponding to Pt (111) is slightly larger than that seen in some studies (0.224 nm^{34, 35}) though it has been shown that strain can increase the lattice spacing for small Pt crystals on carbon supports.³⁶ TGA results for the materials indicate that the Pt wt% for the catalysts was 16.53, 16.07, 15.74 and 15.34% for CB, 350GS, 600GS-CNT and 1000GS-CNT, respectively. HiSPEC 3000, a commercial catalyst, was determined to have a Pt wt% of 20.72%. Figure 5 shows TEM images of the resultant materials following annealing at different magnifications, along with nanocrystal size distributions. Also included is data from the commercial Pt catalyst, HiSPEC 3000. It can be seen from the low magnification TEM images that the distribution of crystals over the surface is not uniform for 350GS and CB,

many regions of the carbon support remain uncovered by Pt crystals. The reason for this might be the formation mechanism and the graphitic quality of the carbon supports. Previous work also indicates that functional groups and defects on the support surface act as nucleation sites to strongly bind Pt crystals.^{37, 38} If the formation mechanism indeed involves the movement of atoms over the surface, it can be expected that the mean free path of these species is decreased on surfaces which are more defective, as is the case with 350GS and CB relative to 600GS-CNT and 1000GS-CNT. Whilst more defective graphitic surfaces are associated with smaller nanocrystals compared to pristine graphitic surfaces when solution based crystal synthesis methods are utilised,³⁷ we find that a wider size distribution with larger crystals are found on 350GS than on the more crystalline GS-CNT surfaces. This could also be attributed to the formation mechanism, once the precursor dries on the carbon surface, it can be expected to form aggregates instead of equally coating the whole of the carbon surface. A low mean free path for Pt atoms will result in large numbers of Pt crystals in close proximity, which could quickly sinter during the 30 minute growth period. Despite the dispersion issues with 350GS and CB, the average nanocrystal diameters for all samples was under 5 nm, though standard deviations in nanocrystals size for 350GS was much larger than for other supports.

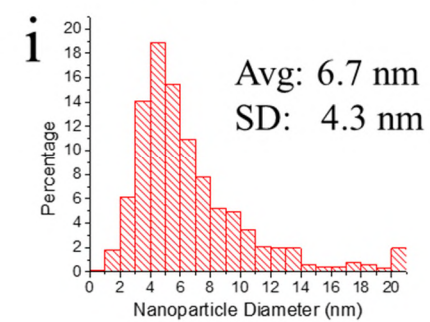
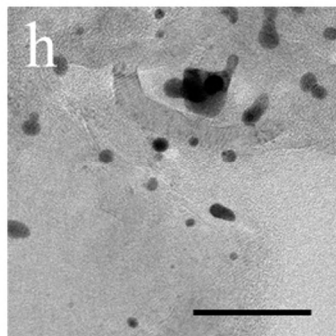
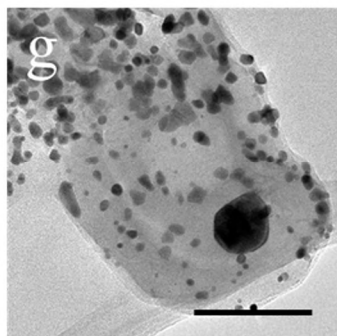
350GS



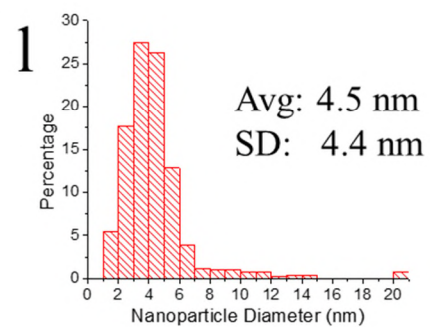
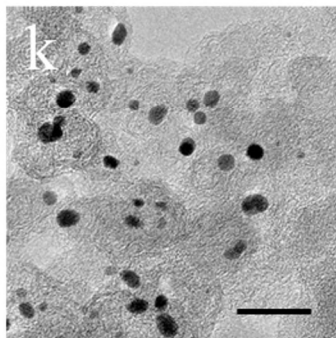
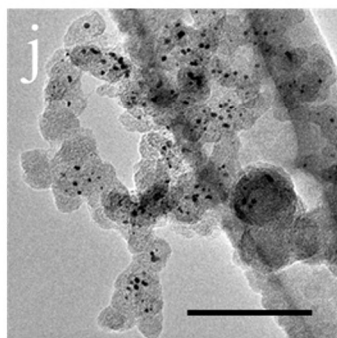
600GS-CNT



1000GS-CNT



CB



HiSPEC 3000

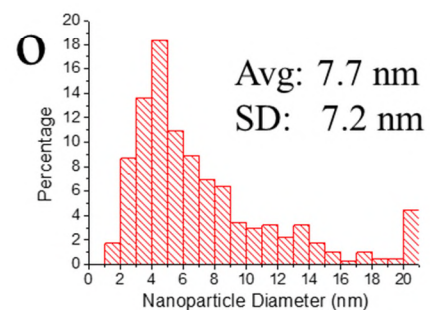
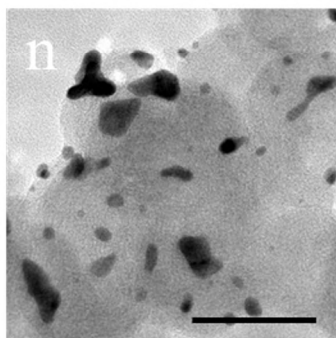
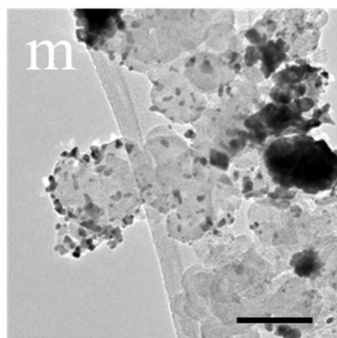


Figure 8. TEM of catalysts after electrochemical cycling. Low magnification images, high magnification TEM images and particle size histograms with averages and standard deviations for 350GS (a-c), 600GS-CNT (d-f), 1000GS-CNT (g-i), CB (j-l) and HiSPEC 3000 (m-o). Nanoparticles with >20 nm diameter are grouped for clarity. Scale bars: (a) 200 nm (b) 50 nm (d) 100 nm (e) 50 nm (g) 100 nm (h) 50 nm (j) 100 nm (k) 20 nm (m) 100 nm (n) 50 nm.

Cyclic voltammetry (CV) measurements were recorded to evaluate the electrochemically active surface areas (ECSAs) and durabilities of the catalysts (see Experimental section). The initial and final ECSAs of the catalysts, along with their cyclic voltammograms and a graph of % ECSA retained following 1000 cycles are shown in Figure 7. The trend for initial ECSA follows the trend $\text{HiSPEC 3000} \approx 600\text{GS-CNT} \approx \text{CB} > 350\text{GS} \approx 1000\text{GS-CNT}$. The final ECSA follows the trend $600\text{GS-CNT} \approx \text{HiSPEC 3000} > 1000\text{GS-CNT} > \text{CB} > 350\text{GS}$. In terms of the relative final ECSA as a percentage of original ECSA, the trend is $600\text{GS-CNT} \approx 1000\text{GS-CNT} \approx \text{HiSPEC 3000} > \text{CB} > 350\text{GS}$. Due to the many differences between the catalysts, for example their surface areas, catalyst size and distribution, support morphologies and the presence of CNTs in varying amounts, it is difficult to attribute the ECSAs and durability to any single factor. It should be noted that the supports with poor initial catalyst dispersion (CB and GS350) had the lowest ECSA both in absolute and relative terms after 1000 cycles, this could be due to poor dispersion resulting in closer crystals, which sinter more rapidly and result in higher ECSA loss.³⁹ The results show that 600GS-CNT had similar initial, final, and relative ECSAs compared to HiSPEC 3000. 1000GS-CNT had a similar final relative ECSA to HiSPEC 3000 and 600GS-CNT, though its low initial ECSA means that it shows inferior performance in absolute terms. Post-cycling TEM results were recorded for each sample (Figure 8). It should be noted that despite the higher average

nanocrystal diameters post-cycling for 600GS-CNT and 1000GS-CNT, these catalysts had higher final ECSAs than CB and 350GS. This indicates superior attachment of crystals in the case of the GS-CNT supports, it should be noted that the population of crystals with sizes >8 nm is very small for CB and 350GS post cycling, indicating that crystals on these supports are more likely to detach from the surface than migrate on the surface compared to GS-CNT supports. Previous work suggests that carbon supports with a higher degree of graphitisation, such as the GS-CNT supports, are more resistant to corrosion in acidic environments,⁴⁰ which is known to contribute to detachment of Pt nanocrystals from carbon surfaces.⁴¹ It would be useful to compare these supports for the growth of Pt crystals via solution methods which can give more uniform Pt crystal size and which could provide better dispersion over 350GS, in order to give greater insight into the role of the support crystallinity in determining catalyst durability.

Procedure

For each experiment, an alumina furnace crucible was half filled (~1.25 g) with nickel acetate tetrahydrate (98%, Sigma-Aldrich). The sample was placed in a 1 inch diameter quartz tube in a horizontal tube furnace. A furnace on rails was used so that the sample could be rapidly introduced and removed from the hot zone of the furnace. Argon (200 sccm) was flowed through the system whilst the furnace reached the desired temperature, during this time the sample was in the room temperature zone of the system unless stated otherwise for certain experiments. For the experiment utilising dehydrated nickel acetate, the nickel acetate was heated for 30 minutes at 100 °C in the tube furnace, before being removed from the hot zone prior to the furnace being heated to the desired temperature. Once the furnace had reached the desired temperature the ceramic boat containing the nickel acetate tetrahydrate was

rapidly introduced into the hot zone of the furnace. Following the desired annealing period the sample was removed from the hot zone of the furnace to allow rapid cooling to room temperature. The system was then cooled back to ambient temperature and the sample removed.

3D CNT-graphene hybrid (600, 700, 800, 900 and 1000GS-CNT): Argon was flowed through the system while the furnace reached 600-1000 °C depending on the desired product, the sample was moved into the hot zone of the furnace for a period of 2 hours unless otherwise stated, after this the sample was removed from the hot zone of the furnace and removed after it had cooled to ambient temperature.

3D graphene spheres (350GS): Argon was flowed through the system while the furnace reached 350 °C, the sample was moved into the hot zone of the furnace for a period of 2 hours unless otherwise stated, after this the sample was removed from the hot zone of the furnace and removed after it had cooled to ambient temperature.

Crystalline 3D graphene spheres (600GS and 1000GS): Argon was flowed through the system while the furnace reached a temperature of 350 °C. The sample was moved into the hot zone of the furnace and annealed for 1 hour, following this the furnace was set to 600 or 1000 °C with a ramp rate of 50 °C/min and the sample was annealed for another hour (including heating time). Following this the sample was removed from the hot zone of the furnace and allowed to cool to room temperature.

Etching of Nickel: For the etching process, the nickel-carbon materials were placed in a solution of 3M Hydrochloric acid (diluted from 37% HCl) and heated for 5 hours at 80°C. The acid was exchanged for fresh 3M HCl and the heating repeated to ensure removal of as much nickel as possible. Following this the product was isolated via centrifugation and washed repeatedly with DI water and then ethanol.

TEM sample preparation: A small amount of product was placed in isopropyl alcohol (or a small amount of water and then isopropyl alcohol for Pt-containing samples) and sonicated for ~15 minutes. Several drops of the sample were then deposited on holey carbon TEM grids. For TEM samples of post-cycled catalysts, the glassy carbon electrode containing the cycled catalyst film was rinsed with IPA and the resultant solution was deposited on a TEM grid.

Nanocrystal measurements: At least 500 nanocrystals were measured for each average value, standard deviation and size distribution both pre- and post-electrochemical cycling.

Synthesis of Pt nanocrystals on carbon supports using thermal annealing: 20mg of 350GS, 600GS-CNT, 1000GS-CNT or carbon black (CB – Vulcan XC72R) was mixed with 0.6 mL of 50mM H_2PtCl_6 (Sigma-Aldrich) in ethanol. This mixture was evaporated at 50 °C overnight on a hot plate. The resultant powder was then introduced into the hot zone of a tube furnace with a 1 in. quartz tube at 400 °C for 30 minutes under a flow of H_2 (20% in argon, 100 sccm) and Argon (200 sccm). Following annealing the sample was removed from the hot zone and the system was cooled to room temperature.

For the cyclic voltammetry (CV) experiments, the catalyst ink was prepared as follows: 7 mg of catalyst was mixed with 400 μL DI water, 1350 μL isopropyl alcohol and 250 μL of 5% Nafion in alcohol solution (Sigma-Aldrich). The mixture was then sonicated using a horn-tip sonicator for 30 minutes with 5 second pulses separated by rest periods of 5 seconds. For each CV measurement, 4 μL of the catalyst ink was pipetted onto a 3 mm glassy carbon electrode which had previously been polished. 0.5 M H_2SO_4 solution was used as the electrolyte in CV measurements, and was purged for 30 minutes with argon prior to measurements. An Ag/AgCl electrode (3M NaCl) and a platinum wire were used as the reference and counter electrodes respectively. CV measurements consisted of an activation

step of 50 cycles between 0.05-1.2V vs RHE at 100 mV/s, before 1000 cycles at 40 mV/s at the same potentials. All CV measurements were recorded using a BioLogic VMP3.

Characterisation: Scanning electron microscope (SEM) images were acquired using a Hitachi S-4300 operated at 3kV and 10kV. Transmission electron microscope (TEM) images were acquired with a JEOL-2100 operated at 200 kV and a JEOL-2200MCO operated at 80 kV. Raman spectra were acquired with a Horiba Labram aramis Raman microscope equipped with a 532 nm laser. BET surface areas were obtained using a Micromeritics Gemini VI BET. Thermogravimetric analysis was carried out using a PerkinElmer Diamond TG/DTA.

Conclusions

We have demonstrated the synthesis of multi-layered graphene spheres and graphene-CNT hybrid materials via annealing of nickel acetate, a cheap and readily available nickel compound. The nickel acetate decomposes to generate the catalyst/template and carbon feedstock in this process in-situ. In the presence of carbon, newly formed nickel particles catalysed the formation of graphene or carbon nanotubes, depending on the conditions. The sudden introduction of the acetate to the hot zone of the furnace was shown to be a key factor in the formation of these structures. This scalable method allows the crystalline quality of the material to be tuned by utilising different annealing times and temperatures, as indicated by TEM and Raman. Using high annealing temperatures, we have shown it is possible to produce materials which comprise high quality multi-layered graphene and CNTs. This method demonstrates a way to produce graphene spheres without requiring pre-formed nickel particles, and allows hybrid materials to be formed in a single step. The possibility of using other metal salts and varying the synthesis conditions may allow materials with other morphologies, decreased layer numbers and substitutional dopant atoms to be fabricated, for

example, using copper salts in conjunction with nickel acetate may facilitate a reduction in layer number, and the addition of solid nitrogen containing nickel precursors such as nickel (II) dimethylglyoxime may allow the formation of crystalline nitrogen-doped graphitic materials. The materials formed may be useful in electrochemical applications, where three-dimensional graphene and graphene-CNT hybrid materials have advantageous properties and where scalable processes are required. We utilised some of these materials as supports for the thermal annealing growth of Pt nanocrystals, where in some cases they exhibited superior performance to Vulcan XC-72 and showed comparable performance to HiSPEC 3000, a commercial catalyst, demonstrating the potential of this synthesis method.

Acknowledgements

H. Kim has been supported by the Research and Development Program of Korea Institute of Energy Research (KIER/B6-2452).

References

- (1) Antolini, E. Graphene as a new carbon support for low-temperature fuel cell catalysts. *Appl. Catal. B-Environ.* **2012**, *123*, 52-68.
- (2) Antolini, E. Carbon supports for low-temperature fuel cell catalysts. *Appl. Catal. B-Environ.* **2009**, *88*, 1-24.
- (3) Kucinskis, G.; Bajars, G.; Kleperis, J. Graphene in lithium ion battery cathode materials: A review. *J. Power Sources* **2013**, *240*, 66-79.
- (4) Zhang, X.; Zhang, H.; Li, C.; Wang, K.; Sun, X.; Ma, Y. Recent advances in porous graphene materials for supercapacitor applications. *RSC Adv.* **2014**, *4*, 45862-45884.
- (5) Lee, J. H.; Park, N.; Kim, B. G.; Jung, D. S.; Im, K.; Hur, J.; Choi, J. W. Restacking-Inhibited 3D Reduced Graphene Oxide for High Performance Supercapacitor Electrodes. *ACS Nano* **2013**, *7* (10), 9366-9374.
- (6) Mao, S.; Lu, G.; Chen, J. Three-dimensional graphene-based composites for energy applications. *Nanoscale* **2015**, *7*, 6924-6943.

- (7) Chen, Z. P.; Ren, W. C.; Gao, L. B.; Liu, B. L.; Pei, S. F.; Cheng, H. M. Three-dimensional flexible and conductive interconnected graphene networks grown by chemical vapour deposition. *Nat. Mater.* **2011**, *10*, 424-428.
- (8) Sha, J.; Gao, C.; Lee, S.-K.; Li, Y.; Zhao, N.; Tour, J. M. Preparation of Three-Dimensional Graphene Foams Using Powder Metallurgy Templates. *ACS Nano* **2016**, *10* (1), 1411-1416.
- (9) Chen, S.; Chen, P.; Wang, Y. Carbon nanotubes grown in situ on graphene nanosheets as superior anodes for Li-ion batteries. *Nanoscale* **2011**, *3*, 4323-4329.
- (10) Liu, J.; Zhang, L.; Wu, H. B.; Lin, J.; Shen, Z.; Lou, X. W. High-performance flexible asymmetric supercapacitors based on a new graphene foam/carbon nanotube hybrid film. *Energy Environ. Sci.* **2014**, *7*, 3709-3719.
- (11) Cheng, Q.; Tang, J.; Ma, J.; Zhang, H.; Shinya, N.; Qin, L.-C. Graphene and carbon nanotube composite electrodes for supercapacitors with ultra-high energy density. *Phys. Chem. Chem. Phys.* **2011**, *13*, 17615-17624.
- (12) Yang, J.; Sun, H.; Liang, H.; Ji, H.; Song, L.; Gao, C.; Xu, H. A Highly Efficient Metal-Free Oxygen Reduction Electrocatalyst Assembled from Carbon Nanotubes and Graphene. *Adv. Mater.* **2016**, *28*, 4606-4613.
- (13) Stephens, I. E. L.; Bondarenko, A. S.; Grønbjerg, U.; Rossmeisl, J.; Chorkendorff, I. Understanding the electrocatalysis of oxygen reduction on platinum and its alloys. *Energy Environ. Sci.*, **2012**, *5*, 6744-6762.
- (14) Sheng, W. C.; Gasteiger, H. A.; Shao-Horn, Y. J. Hydrogen Oxidation and Evolution Reaction Kinetics on Platinum: Acid vs Alkaline Electrolytes. *Electrochem. Soc.* **2010**, *157* (11), B1529-B1536.
- (15) De Jesus, J. C.; González, I.; Quevedo, A.; Puerta, T. Thermal decomposition of nickel acetate tetrahydrate: an integrated study by TGA, QMS and XPS techniques. *Journal of Molecular Catalysis A: Chemical* **2005**, *228*, 283-291.
- (16) Kumar, M.; Ando, Y. Chemical Vapor Deposition of Carbon Nanotubes: A Review on Growth Mechanism and Mass Production. *J. Nanosci. Nanotechnol.* **2010**, *10* (6), 3739-3758.
- (17) Mattevi, C.; Kim, H.; Chhowalla, M. A review of chemical vapour deposition of graphene on copper. *J. Mater. Chem.* **2011**, *21*, 3324-3334.
- (18) Nikolaev, P.; Bronikowski, M. J.; Bradley, R. K.; Rohmund, F.; Colbert, D. T.; Smith, K. A.; Smalley, R. E. Gas-phase catalytic growth of single-walled carbon nanotubes from carbon monoxide. *Chem. Phys. Lett.* **1999**, *313* (1-2), 91-97.
- (19) Losurdo, M.; Giangregorio, M. M.; Capezzuto, P.; Bruno, G. Graphene CVD growth on copper and nickel: role of hydrogen in kinetics and structure. *Phys. Chem. Chem. Phys.* **2011**, *13*, 20836-20843.

- (20) Behr, M. J.; Gaulding, E. A.; Mkhoyan, K. A.; Aydil, E. S. Effect of hydrogen on catalyst nanoparticles in carbon nanotube growth. *J. Appl. Phys.* **2010**, *108*, 053303.
- (21) Baraton, L.; He, Z. B.; Lee, C. S.; Cojocaru, C. S.; Châtelet, M.; Maurice, J. L.; Lee, Y. H.; Pribat, D. On the mechanisms of precipitation of graphene on nickel thin films. *Europhys. Lett.* **2011**, *96*, 46003.
- (22) Goh, B.-M.; Wang, Y.; Reddy, M. V.; Ding, Y. L.; Lu, L.; Bunker, C.; Loh, K. P. Filling the Voids of Graphene Foam with Graphene “Eggshell” for Improved Lithium-Ion Storage. *ACS Appl. Mater. Interfaces* **2014**, *6*, 9835-9841.
- (23) Sun, Z. Z.; Yan, Z.; Yao, J.; Beitler, E.; Zhu, Y.; Tour, J. M. Growth of graphene from solid carbon sources. *Nature* **2010**, *468*, 549-552.
- (24) Galwey, A. K.; McKee, S. G.; Mitchell, T. R. B.; Brown, M. E.; Bean, A. F. A kinetic and mechanistic study of the thermal decomposition of nickel acetate. *React. Solids* **1988**, *6*, 173-186.
- (25) Mohamed, M. A.; Halawy, S. A.; Ebrahim, M. M. Non-isothermal decomposition of nickel acetate tetrahydrate. *J. Anal. Appl. Pyrolysis* **1993**, *27*, 109-118.
- (26) Bayer, B. C.; Bosworth, D. A.; Michaelis, F. B.; Blume, R.; Habler, G.; Abart, R.; Weatherup, R. S.; Kidambi, P. R.; Baumberg, J. J.; Knop-Gericke, A.; Schloegl, R.; Baecht, C.; Barber, Z. H.; Meyer, J. C.; Hoffman, S. In Situ Observations of Phase Transitions in Metastable Nickel (Carbide)/ Carbon Nanocomposites. *J. Phys. Chem. C* **2016**, *120* (39), 22571-22584.
- (27) Shibuta, Y.; Elliott, J. A. Interaction between graphene and nickel(111) surfaces with commensurate and incommensurate orientational relationships. *Chem. Phys. Lett.* **2012**, *538*, 112-117.
- (28) Hayashi, T.; O'Connor, T. C.; Higashiyama, K.; Nishi, K.; Fujisawa, K.; Muramatsu, H.; Kim, Y. A.; Sumpter, B. G.; Meunier, V.; Terrones, M.; Endo, M. A reversible strain-induced electrical conductivity in cup-stacked carbon nanotubes. *Nanoscale* **2013**, *5*, 10212-10218.
- (29) Spyrou, K.; Rudolf, P. An Introduction to Graphene. In *Functionalization of Graphene*, Wiley-VCH Verlag GmbH & Co. KGaA: Weinheim, 2014; pp 1-20.
- (30) Worsley, M. A.; Pham, T. T.; Yan, A.; Shin, S. J.; Lee, J. R. I.; Bagge-Hansen, M.; Mickelson, W.; Zettl, A. Synthesis and Characterization of Highly Crystalline Graphene Aerogels. *ACS Nano* **2014**, *8* (10), 11013-11022.
- (31) Li, Y.; Zhang, X. B.; Tao, X. Y.; Xu, J. M.; Huang, W. Z.; Luo, J. H.; Luo, Z. Q.; Li, T.; Liu, F.; Bao, Y.; Geise, H. J. Mass production of high-quality multi-walled carbon nanotube bundles on a Ni/Mo/MgO catalyst. *Carbon* **2005**, *43*, 295-301.
- (32) Yoon, S.-M.; Choi, W. M.; Baik, H.; Shin, H.-J.; Song, I.; Kwon, M.-S.; Bae, J. J.; Kim, H.; Lee, Y. H.; Choi, J.-Y. Synthesis of Multilayer Graphene Balls by Carbon Segregation from Nickel Nanoparticles. *ACS Nano* **2012**, *6* (8), 6803-6811.

- (33) Siburian, R.; Nakamura, J. Formation Process of Pt Subnano-Clusters on Graphene Nanosheets. *J. Phys. Chem. C* **2012**, *116* (43), 22947-22953.
- (34) Ding, D.; Song, Z. L.; Cheng, Z. Q.; Liu, W. N.; Nie, X. K.; Bian, X.; Chen, Z.; Tan, W. H. Plasma-assisted nitrogen doping of graphene-encapsulated Pt nanocrystals as efficient fuel cell catalysts. *J. Mater. Chem. A* **2014**, *2*, 472-477.
- (35) Zhang, B.; Wang, D.; Hou, Y.; Yang, S.; Yang, X. H.; Zhong, J. H.; Liu, J.; Wang, H. F.; Hu, P.; Zhao, H. J.; Yang, H. G. Facet-Dependent Catalytic Activity of Platinum Nanocrystals for Triiodide Reduction in Dye-Sensitized Solar Cells. *Sci. Rep.* **2013**, *3*, 1836
- (36) Daio, T.; Staykov, A.; Guo, L.; Liu, J.; Tanaka, M.; Matthew Lyth, S.; Sasaki, K. Lattice Strain Mapping of Platinum Nanoparticles on Carbon and SnO₂ Supports. *Sci Rep* **2015**, *5*, 13126
- (37) Xin, L.; Yang, F.; Rasouli, S.; Qiu, Y.; Li, Z.-F.; Uzunoglu, A.; Sun, C.-J.; Liu, Y.; Ferreira, P.; Li, W.; Ren, Y.; Stanciu, L. A.; Xie, J. Understanding Pt Nanoparticle Anchoring on Graphene Supports through Surface Functionalization. *ACS Catal.* **2016**, *6* (4), 2642-2653.
- (38) Fampiou, I.; Ramasubramaniam, A. Binding of Pt Nanoclusters to Point Defects in Graphene: Adsorption, Morphology, and Electronic Structure. *J. Phys. Chem. C* **2012**, *116* (11), 6543-6555.
- (39) Meier, J. C.; Galeano, C.; Katsounaros, I.; Witte, J.; Bongard, H. J.; Topalov, A. A.; Baldizzone, C.; Mezzavilla, S.; Schüth, F.; Mayrhofer, K. J. J. Design criteria for stable Pt/C fuel cell catalysts. *Beilstein J. Nanotechnol.* **2014**, *5*, 44-67.
- (40) Castanheira, L.; Silva, W. O.; Lima, F. H. B.; Crisci, A.; Dubau, L.; Maillard, F. Carbon Corrosion in Proton-Exchange Membrane Fuel Cells: Effect of the Carbon Structure, the Degradation Protocol, and the Gas Atmosphere. *ACS Catal.* **2015**, *5* (4), 2184-2194.
- (41) Mayrhofer, K. J. J.; Ashton, S. J.; Meier, J. C.; Wiberg, G. K. H.; Hanzlik, M.; Arenz, M. Non-destructive transmission electron microscopy study of catalyst degradation under electrochemical treatment. *J. Power Sources* **2008**, *185* (2), 734-739.